Aeolian Research 61 (2023) 100867

Contents lists available at ScienceDirect

Aeolian Research

journal homepage: www.elsevier.com/locate/aeolia

How wind direction and building spacing influences airflow patterns and sediment transport patterns around a row of beach buildings: A numerical study

Paran Pourteimouri *, Geert H.P. Campmans, Kathelijne M. Wijnberg, Suzanne J.M.H. Hulscher

Water Engineering and Management, Faculty Engineering Technology, University of Twente, P.O. Box 217, 7500AE Enschede, The Netherlands

ARTICLE INFO

Keywords:
Airflow around buildings
Aeolian sediment transport
Erosion and deposition patterns
Buildings positioning at beach
Computational fluid dynamics (CFD)

ABSTRACT

Buildings at the beach change the near-bed airflow patterns in the surrounding area. This induces alterations in wind-induced bed shear stress and wind-induced sediment transport which, in turn, affect the bed topography in the vicinity of buildings. Three-dimensional computational fluid dynamics simulations using OpenFOAM have been performed to understand how and to what extent the buildings at the beach influence the sediment transport from the beach to the dunes. Herein, we explicitly account for the positioning of the buildings with respect to each other and the dominant wind direction. Also discussed are the airflow mechanisms that are responsible for sediment transport, and how they alter due to systematic changes in the gap spacing between buildings and the wind incidence angle. Simulations were performed, in which we model flow and initial sediment transport around a repeating row of ten parallel full-scale beach buildings when the gap spacings and wind incidence angles were systematically varied. The horizontal near-bed streamline patterns showed that there is a critical gap spacing, below which the neighboring buildings significantly affect each other. Furthermore, the airflow in the near-wake region behind the row of buildings is quite complex. The shape and the extent to which the sand drifts develop behind the gaps between buildings are largely influenced by the wind direction, relative to the buildings. We also computed the average sediment transport flux along different lines downstream of the buildings. Our findings showed that, depending on the buildings' positioning at the beach, they could have negative effects on dune growth by obstructing the sediment particles from moving downstream, or they could have positive effects on dune growth by steering the airflow and supplying more sediment downstream.

Introduction

The recreational value and attractiveness of sandy beaches worldwide, makes the understanding of the influence that buildings might have in the surrounding area vital. Buildings by the beach such as hotels, holiday cottages, restaurants, sailing and surfing clubs, lifeguard rescue towers and pavilions (Fig. 1) affect the near-bed wind field due to their size, shape, elevation from the bed, construction materials and their location on the beach (Nordstrom and McCluskey 1985; Nordstrom, 2004; Jackson and Nordstrom, 2011). The sediment mass transport in sandy environments, such as beaches, depends on complex interactions between near-bed wind field, sediment transport and instantaneous changes in bed morphology (Walker and Nickling, 2002). Therefore, in response to the spatial variations in near-bed flow dynamics due to the protrusion of buildings into the near-bed boundary layer, erosion and deposition patterns develop. These building-induced erosion and deposition patterns might become problematic over a longer time-scale. Buildings change the wind-blown sediment supply moving from the beach towards the dunes and might affect the flood safety functioning of the dunes (Nordstrom and McCluskey, 1984; Nordstrom and Jackson, 1998).

Furthermore, the scouring and sediment trapping around buildings could cause structural malfunction (Jackson and Nordstrom, 2011). A quantitative study on the impact of building spacing in rows of beach houses, and the prevailing wind direction on near-bed wind field as well as erosion and deposition patterns would be of interest for coastal engineers, morphologists, and owners of the buildings. The findings of such a study could provide scientific support for coastal managers to mitigate threats to both buildings and dunes, in addition to minimizing the need for additional preservation measures.

* Corresponding author.
E-mail address: p.pourteimouri@utwente.nl (P. Pourteimouri).

https://doi.org/10.1016/j.aeolia.2023.100867
Received 11 July 2022; Received in revised form 26 February 2023; Accepted 1 March 2023
Available online 7 March 2023

The airflow patterns around cuboid structures, such as buildings, have been studied extensively through experimental measurements and numerical simulations (Hunt et al., 1978; Beranek 1984; Peterka et al., 1985; Martinuzzi and Tropea, 1993; Shah and Ferziger, 1997; Lakehal and Rodi 1997; Chou and Chao 2000; Iaccarino et al., 2003; Gao and Chow, 2005; Yakhot et al., 2006; Pourteimouri et al., 2021). Understanding the aeolian sediment transport and morphological changes around cuboid buildings that are located on movable substrate, e.g. sandy beaches, has been of great interest in previous studies. In case of a sufficiently strong wind, the sediment particles are entrained by the airflow. They strike the windward face of the building, rebound back, and settle in the decelerated flow region at some distance in front of the building where the approaching wind and the reversed flow meet (Bagnold, 1941). The upwind deposition is similar to the so-called echo dunes that also develop in front of the vertical natural obstructions, e.g. cliffs, in sandy environments (Tsoar, 1983; Cooke et al., 1993; Jackson and Nordstrom, 2011; Qian et al., 2011). The sediment accumulation in front of the building grows in size until its slope stands at the angle of repose of dry sand, approximately 34° (Bagnold, 1941). When the equilibrium is reached, additional sediment particles moving towards the windward face of the building slide down the slope of the upwind deposition and join the sediment streams passing around the lateral walls of the building. They are then deposited in two tails starting at a small distance from the lateral walls of the building, and apparently follow the horseshoe-shape vortex downstream of the building (Bagnold, 1941; Pye and Tsoar, 1990; Poppema et al., 2021; Pourteimouri et al., 2021). These two deposition tails gradually merge as the two opposed reversing vortices in the low-speed cavity region carry the sediment particles from the deposition tails towards the middle of the leeward face of the building and create the so-called sand shadow immediately behind the building (Bagnold, 1941; Pye and Tsoar, 1990; Livingstone and Warren, 1996; Luo et al., 2012). Furthermore, previous studies showed that the most intensive erosion occurs around the windward edge and corners of the building (Iversen et al., 1991; Tominaga et al., 2018; Pourteimouri et al., 2021).

Previous studies have examined morphological changes around buildings, while little attention has been paid to how and to what extent these changes depend on the positioning of buildings at the beach. The incident wind direction with respect to the buildings strongly influences the characteristics of the secondary flow patterns in the near-wake region which, in turn, determine the generation and development of sand shadows in the lee of buildings (Cooke et al., 1993; Becker et al., 2002;

Fig. 1. Examples of some buildings at the a, b) Kijkduin, and c, d, e) Katwijk beach, the Netherlands.

Luo et al., 2012; Unnikrishnan et al., 2017). In real beach conditions, buildings are mainly positioned close to each other due to the growth of beach tourism and high demand for centralized facilities on the limited land space at the beach. The wind is slightly accelerated through the gap spacing between adjacent buildings due to the funneling effect. This increases the sediment-entraining capacity of the air. In the lee of the gap, the air decelerates as it flows in a larger space and joins the undisturbed flow sufficiently downstream of the buildings. As a result, the sediment will deposit and form the so-called sand drift at a small distance downstream of the gap (Bagnold, 1941; Pye and Tsoar, 1990; Cooke et al., 1993; Luo et al., 2014; Luo et al., 2016; Poppema et al., 2022). First attempts to systematically study the impact of building positioning with respect to neighboring buildings and the prevailing wind on flow characteristics and the implications for sediment transport go back to the wind-tunnel studies by Luo et al. (2012), Luo et al. (2014) and Luo et al. (2016). However, they only focused on the near-wake flow region, and mainly on the airflow mechanisms responsible for the formation and evolution of sand shadow and sand drift that develop just behind the building, and in the lee of the gap spacing between neighboring buildings, respectively. In a recent study by Poppema et al., 2022; a series of field experiments was performed to study how the initial morphological changes around scaled buildings at the beach are influenced by buildings positioning. An analysis considering real beach conditions, a systematic study around full-scale buildings in a row when the gap spacing between neighboring buildings and the angle of wind incidence are changed over a wide range is lacking so far.

This study aims to answer the following research questions: Q1) How do the flow mechanisms that are responsible for sediment transport around a row of full-scale buildings at the beach change when the gap spacing between neighboring buildings increases?; Q2) How do the flow mechanisms that are responsible for sediment transport around a row of full-scale buildings at the beach change when the wind incidence angle relative to the buildings changes?; Q3) How and to what extent is the potential sediment supply from beach to downstream (towards dunes in real beach) influenced by the buildings positioning at the beach? For the latter research question, we will only study the combined impacts of the buildings spacing in the row and their orientation with respect to the dominant wind.

The present study investigates how the flow mechanisms and the initial morphological patterns around a row of full-scale buildings at the beach, are affected by the gap spacing between neighboring buildings and the wind direction. For this purpose, the OpenFOAM software is used. The choice of methods and model specifications were extensively elaborated by Pourteimouri et al. (2021).

This paper is organized as follows. In section 2, the model descriptions and methods used in this study are presented. Results on the impact of gap spacing and wind incidence angle on near-bed horizontal flow patterns are presented in section 3.1. In section 3.2, the wind-induced bed shear stress due to variations in gap spacing and wind incidence angle are presented. The sediment transport flux is then computed and the duneward component (in x direction) for variations in gap spacing and wind incidence angle is presented in section 3.3. In section 3.4, the initial changes in bed elevation are presented. The paper ends with discussion and conclusions that are presented in section 4 and section 5, respectively.

Methodology

Model specifications

In this study, the three-dimensional OpenFOAM model in Pourteimouri et al. (2021) is further modified to simulate the flow mechanisms around a row of ten full-scale beach buildings. The gap spacing between adjacent buildings and the prevailing wind direction with respect to the buildings is systematically changed. The simpleFOAM solver is selected, which solves the steady Reynolds-averaged Navier-Stokes (RANS) equations for incompressible turbulent flows, using the finite volume method (FVM). The SIMPLE (Semi-Implicit Method for Pressure-Linked Equations) algorithm is used to solve the model equations. The standard $k-\varepsilon$ turbulence closure model is used to solve the turbulence in the vicinity of buildings. The configuration of the computational domain with a row of ten full-scale beach buildings is shown in Fig. 2. Dimensions of the computational domain and beach buildings used in this study are summarized in Table 1. The blockMesh utility of OpenFOAM is used to generate grids with the size of $\Delta x = \Delta y = \Delta z = 1$ m within the entire computational domain. The snappyHexMesh utility is then used to refine the mesh in a bounding box with the height of 9 m from the bed surface. The grid cells in the refinement region are refined four times as they get closer to the buildings. This ends to the cells with the size of $\Delta x = \Delta y = \Delta z = 0.0625$ m close to the buildings. The total number of computational grids in the domain is approximately 3.5 million that mainly consists of hexahedra cells and some polyhedra cells connecting the coarse to fine cells together.

As shown in Fig. 2, the fully-developed profiles of logarithmic wind velocity, U, and turbulence parameters, k and ε, are applied as the inlet boundary conditions using the equations proposed by Richards and Hoxey (1993). The reference wind speed of $u_{ref} = 17$ m/s is considered at the reference height of $z_{ref} = 1.8$ m above the ground level, $z = 0$ m, to prescribe the logarithmic velocity profile at the inlet of the domain. A uniform surface roughness height of $z_0 = 0.00001$ m is applied at the bottom of the domain, which was computed based on the median sediment grain size at the beach (3.00×10^{-4} m). The open boundary condition with zero-gauge pressure is considered at the outlet of the domain. At the spanwise boundaries of the domain, the cyclic (periodic) boundary condition is used to assure that the flow conditions are periodically repeating between these two boundaries, allowing the incident wind to make an angle with the centerline of the buildings (x-direction). Another advantage of using the cyclic lateral boundaries is that it reproduces the actual beach situation where the row of buildings is repetitively placed at the beach. It should be noted that we assumed a constant domain width, meaning that by increasing the gap size between neighboring buildings in the row, we reduce the distance between the neighboring rows of buildings. Furthermore, the no-slip velocity boundary condition is used at the bottom of the domain and the buildings' walls. The wall functions are used to accurately resolve the steep gradients of the flow velocity close to the walls. The log-law of the wall for turbulent flow around the buildings is used that significantly reduces the requirements for high grid resolution in the near-wall region. This is achieved by locating the first cell centroid off the wall in the log-law region of the boundary layer, $y^+ > 30$, instead of the linear viscous sub-layer, $y^+ < 5$ (Blocken et al., 2007). More detailed information on the model specifications, the implementation of boundary conditions and wall functions can be found in Pourteimouri et al. (2021).

Model setup for spacing and orientations scenario's

To systematically evaluate the impact of gap spacing between neighboring beach buildings on flow mechanisms and morphological changes around buildings, 16 different simulations were performed, in which the gap spacing between buildings increased from 0.1 to 4 times the width of each building. Similar to the previous studies by Luo et al. (2014) and Luo et al. (2016), a dimensionless parameter, the gap ratio, was used in the present study. When considering equal distances between neighboring beach buildings in the row, the gap ratio, $g^* = s/(s + w)$, denotes the ratio of the gap spacing between buildings to the center-to-center distance between buildings (Fig. 3). The wind incidence angle, θ_w, represents the angle between the prevailing wind direction and the centerline of the buildings (Fig. 3). To understand how the airflow patterns and the bed level change around beach buildings are influenced by the wind incidence angle, five different wind directions, 0°, 20°, 40°, 60° and 80°, were applied for each tested gap ratio. An overview of the

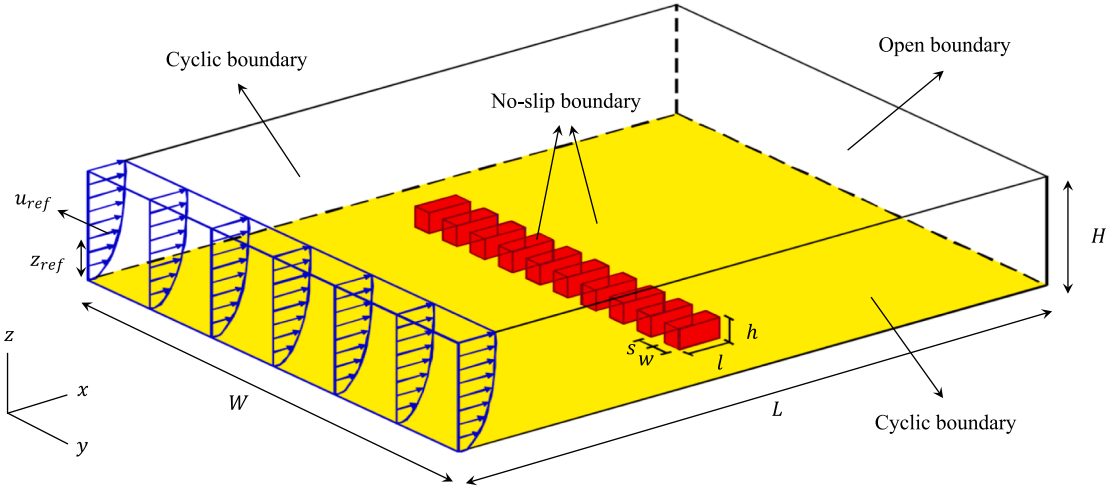

Fig. 2. Schematization of the modelled beach buildings within the computational domain. The domain inlet is located at $x = 0$ m, and the incident wind is perpendicular to the upwind (seaward) face of buildings.

Table 1
Geometric dimensions of the computational domain and beach buildings.

Variable	Value [m]
Length of the domain (***L***)	150.00
Width of the domain (***W***)	150.00
Height of the domain (***H***)	50.00
Length of beach buildings (***l***)	6.00
Width of beach buildings (***w***)	2.50
Height of beach buildings (***h***)	2.50
Gap spacing between neighboring buildings (***s***)	0.25 –10.00

total 80 conducted simulations is given in Table 2.

Sediment transport flux

In sandy substrate such as beaches, the wind-blown sediment transport initiates when the wind shear velocity, $\overrightarrow{u_*}$, exceeds a certain threshold shear velocity, u_{*th}. The commonly used aeolian sediment transport models based on the experimental measurements show that the equilibrium (saturated) sediment transport flux, $\overrightarrow{q}$, is a function of wind shear velocity and threshold shear velocity (Bagnold, 1937; Kawamura, 1951; Hsu, 1971; Lettau and Lettau, 1977; Horikawa et al., 1983). In this study, sediment transport was modelled using the transport formulation proposed by Bagnold (1937) as follows:

$$\overrightarrow{q} = C\frac{\rho_a}{g}\sqrt{\frac{d}{D}}(|\overrightarrow{u_*}| - u_{*th})^3\frac{\overrightarrow{u_*}}{|\overrightarrow{u_*}|} \tag{1}$$

where $\overrightarrow{q}[kg/ms]$ is the sediment transport flux; $C[-]$ is an empirical constant related to the sediment particle size distribution, ranging from 1.50 for nearly uniformly distributed sediment particles to 2.80 for widely distributed sediment particles; $\rho_a[kg/m^3]$ is the density of air $(1.29kg/m^3)$, $g[m/s^2]$ is the gravitational acceleration, $d[m]$ is the nominal sediment particle size $(3.00 \times 10^{-4}$ m); $D[m]$ is the reference sediment particle size $(2.40 \times 10^{-4}$ m); $\overrightarrow{u_*}[m/s]$ is the wind shear velocity; and $u_{*th}[m/s]$ is the threshold shear velocity. The wind shear velocity, $\overrightarrow{u_*}$, is calculated by:

$$\overrightarrow{u_*} = \sqrt{\frac{|\overrightarrow{\tau}|}{\rho_a}}\frac{\overrightarrow{\tau}}{|\overrightarrow{\tau}|} \tag{2}$$

where $\overrightarrow{\tau}[N/m^2]$ is the wind shear stress calculated at the bed of the computational domain by solving the flow field using the airflow model used in this study, OpenFOAM. The post-processing techniques provided by OpenFOAM was used to extract the results of the bed shear stress ($z = 0$ m) at the center of each grid cell across the entire domain.

As the wind-induced drag and lift forces on sediment particles increase, there is a critical shear velocity at which the sediment particles start moving. This threshold shear velocity, u_{*th}, is derived by Bagnold

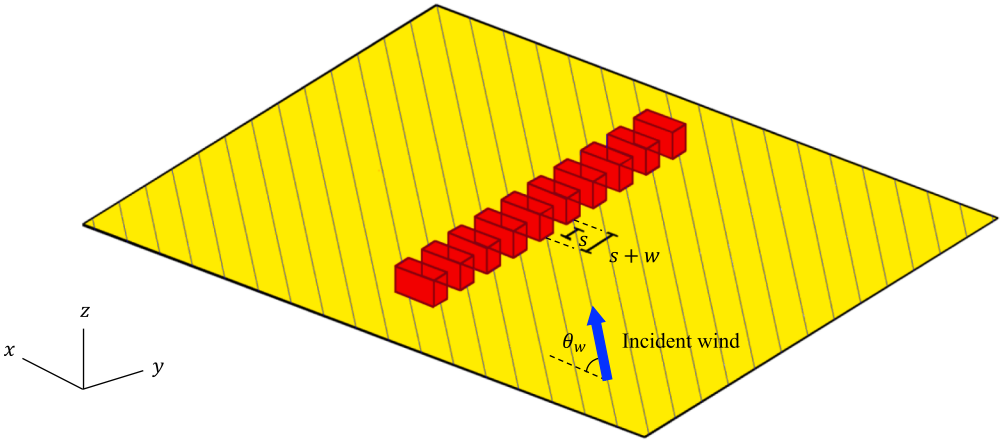

Fig. 3. Illustration of the prevailing wind in the domain, wind incidence angle, θ_w, and the parameters used to characterize the gap ratio, g^*.

Table 2
Parameters of the total 80 conducted simulations.

Dimensionless gap Spacing, s/w [−]	Gap Ratio, g^* [−]	Wind Incidence Angle, θ_w [°]
0.10	0.09	0, 20, 40, 60, 80
0.20	0.17	0, 20, 40, 60, 80
0.30	0.23	0, 20, 40, 60, 80
0.40	0.29	0, 20, 40, 60, 80
0.50	0.33	0, 20, 40, 60, 80
0.60	0.37	0, 20, 40, 60, 80
0.70	0.41	0, 20, 40, 60, 80
0.80	0.44	0, 20, 40, 60, 80
0.90	0.47	0, 20, 40, 60, 80
1.00	0.50	0, 20, 40, 60, 80
1.50	0.60	0, 20, 40, 60, 80
2.00	0.67	0, 20, 40, 60, 80
2.50	0.71	0, 20, 40, 60, 80
3.00	0.75	0, 20, 40, 60, 80
3.50	0.78	0, 20, 40, 60, 80
4.00	0.80	0, 20, 40, 60, 80

(1937) as:

$$u_{*th} = A\sqrt{\frac{\rho_s - \rho_a}{\rho_a} g d} \tag{3}$$

where A is an empirical constant dependent on the sediment particle size; and $\rho_s[kg/m^3]$ is the density of sediment $(2.65 \times 10^3 kg/m^3)$. The value of A is 0.1 for sediment particles greater than 8.00×10^{-5} m (Nickling and Neuman, 2009).

The sediment transport flux, $\vec{q}$, represents the sediment-carrying capacity of incident wind parallel to the wind direction. In order to predict the potential of wind to move sediments in the cross-shore direction and towards the dune, the x component of $\vec{q}$ is derived using the local wind incidence angles as (Bauer and Davidson-Arnott, 2003; Delgado-Fernandez and Davidson-Arnott, 2011):

$$q_c = |\vec{q}|.\cos\theta_{wl} \tag{4}$$

where $q_c[kg/ms]$ is the sediment transport flux in the cross-shore direction (x component of $\vec{q}$); and θ_{wl} is the local wind direction at each computational grid.

Initial erosion and deposition patterns

In this study, we are investigating how the potential morphological changes around beach buildings are influenced by the gap spacing between buildings and by the wind incidence angle. To evaluate the areas at which the sediment particles are eroded or deposited around beach buildings, the Exner equation is used, which describes the mass balance between the deposited sediment on the bed and the sediment in transport. The general form of the Exner equation is as follows (Paola and Voller, 2005; Bauer et al., 2015):

$$\frac{\partial z_b}{\partial t} = -\frac{1}{\rho_s(1-n)}\vec{\nabla}\cdot\vec{q} \tag{5}$$

where $z_b[m]$ is the bed level; $t[s]$ is the time; and $n[-]$ is the sediment porosity (0.4). The equation states that the rate of changes in bed level through time is proportional to the spatial divergence of the sediment transport flux.

Results

Near-bed horizontal flow patterns

Impact of gap spacing

Fig. 4 shows the horizontal near-bed streamline patterns around a row of ten full-scale beach buildings for different gap ratios, g^*, when the incident wind is perpendicular to the front face of the buildings, $\theta_w = 0^\circ$. It should be noted that in computations of the streamlines, the z component of the velocity was not taken into account. For the sake of brevity, among sixteen different tested gap ratios, only the results for the five most important ones, consisting 0.09, 0.41, 0.47, 0.50 and 0.67 are presented. These figures show that the flow patterns downstream of the buildings are complex, and depend on the gap ratio between neighboring buildings. This is due to the interactions between the jet flows passing through the gap spacings between buildings and the deflected flows due to the presence of buildings, moving around the lateral faces of the buildings. The near-wake streamline patterns shown in Fig. 4 are comparable with those observed for two adjacent wide rectangular obstacles in wind-tunnel experiments by Luo et al. (2014).

For small gap spacing, $g^* = 0.09$, the row of ten buildings effectively forms one wide rectangular bluff body for the approaching wind. The jet

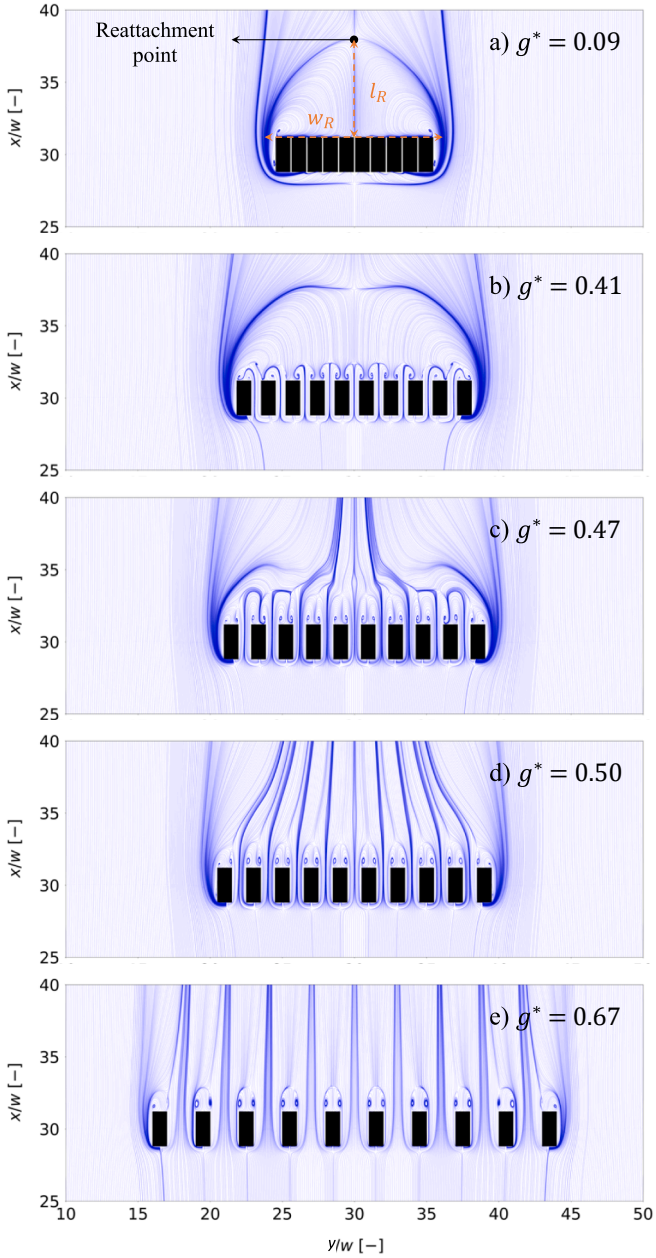

Fig. 4. Horizontal airflow patterns at a near-bed plane, $z = 0.25$ m, for $\theta_w = 0^\circ$, and the gap ratio, g^*, is changed as a) 0.09, b) 0.41, c) 0.47, d) 0.50 and e) 0.67.

flows passing through the small gap spacings between buildings are negligible and the airflow is mainly split at the upwind face of the bluff body, moving towards the lateral faces, see Fig. 4a. The deflected flows are separated from the sharp trailing corners of the bluff body and form a pair of large opposing vortices in the low-pressure zone just behind the lee face of the body. The approximate longitudinal and spanwise dimensions of the downwind recirculation region are $l_R = 6.9w$ and $w_R = 10.98w$, respectively. It should be noted that the location of the flow reattachment point, shown in Fig. 4a, is determined by examining where the streamwise velocity component, u, of the flow along the centerline of the central gap spacing between buildings changes in sign from negative to positive at $z = 0.25$ m. The length of the recirculation region, l_R, was then computed as the distance between the reattachment point and the lee face of the buildings. Furthermore, the width of the recirculation region, w_R, was computed as the length of the line that connects the outer edges of the opposing vortices, and is located just behind the lee face of the buildings (see Fig. 4a).

As the gap ratio increases to $g^* = 0.41$, the jet flows through the gap spacings between neighboring buildings are enhanced. Jet flows are detached from the surface when they encounter the sharp lee corners of the buildings and inclined into different directions by the Coanda effect (Yen and Liu, 2011). Therefore, two small counter-rotating vortices are formed immediately downstream of the gaps. These smaller size vortices are encompassed with a pair of larger vortices that are formed by the deflected flows around the row of buildings, shown in Fig. 4b. It is notable that the flow reattachment point appears at a closer distance from the downwind faces of the buildings, and the approximate streamwise length of the separation bubble decreases to $l_R = 6.5w$.

The jet flows through the gap spacings between buildings become more pronounced and the small vortices that form in the near-wake region just behind the gaps grow in size as the gap ratio increases. For $g^* = 0.47$, the jet flows become intense enough to maintain their initial direction for a longer distance downstream of the buildings and disturb the pair of larger vortices that surrounded the buildings row as whole. As shown in Fig. 4c, the lee streamlines are intertwined due to the confluence of the jet flows and the deflected flows. In addition, the smaller vortices move from just behind the gap to just behind the leeward face of the buildings, and form individual recirculation regions behind each building.

The impact of neighboring buildings on each other becomes less as the gap ratio increases. For $g^* = 0.50$, the jet flows are slightly inclined inward, and the downstream streamlines are compressed (Fig. 4d). For far enough apart buildings with $g^* \geq 0.67$, the jet flows stay parallel to the incident wind, therefore the near-bed flow patterns can be regarded almost independently from neighboring buildings (Fig. 4e).

The near-bed streamwise velocity distribution along the centerline of the central gap spacing between buildings for eight different gap ratios and $\theta_w = 0^\circ$ is shown in Fig. 5. Also indicated in Fig. 5, the streamwise velocity upstream of the buildings decreases dramatically for the closely spaced buildings. For $g^* \leq 0.29$, a small reverse-flow region forms in front of the central gap. As g^* decreases to 0.09, the upwind streamwise velocity reaches its minimum value at $x = 28.30w$, and its magnitude is approximately 1/20 th of the free stream velocity far enough upstream of the row of buildings.

The funneling effect through the gap spacing between buildings causes the streamwise velocity to increase at the beginning of the gap. For $g^* \leq 0.50$, the larger the gap ratio, the farther and the greater maximum streamwise velocity through the central gap. The peak streamwise velocity through the central gap appears at $x = 28.84w$ when $g^* = 0.09$, and it increases by about 12 times at $x = 29.55w$ as g^* increases to 0.50. The streamwise velocity then begins to decrease right after the maximum to some distance downstream of the gap, and then increases to join the undisturbed flow far enough downstream of the buildings. For $g^* \leq 0.47$, the streamwise velocity becomes negative, immediately behind or at some distance downstream of the central gap, depending on the prominence of the smaller vortices just behind the gap, and the pair of large counter-rotating vortices that form behind the row of buildings. The smaller the gap size, the smaller the minimum streamwise velocity, and the minimum is located closer with respect to the lee of the central gap as shown in Fig. 5. For instance, the minimum streamwise velocity appears at $x = 33.30w$ for $g^* = 0.09$, versus $x = 35.30w$ for $g^* = 0.50$.

For $g^* = 0.67$ at which the neighboring buildings are far enough apart to be considered almost independent from each other (Fig. 4e), the decrease in streamwise velocity both in configurations with smaller g^*. In addition, for $g^* \geq 0.67$, the funneling effect through the central gap decreases, therefore the streamwise velocity increases less significantly through the gap. For instance, the difference between the maximum streamwise velocity through the central gap and the minimum

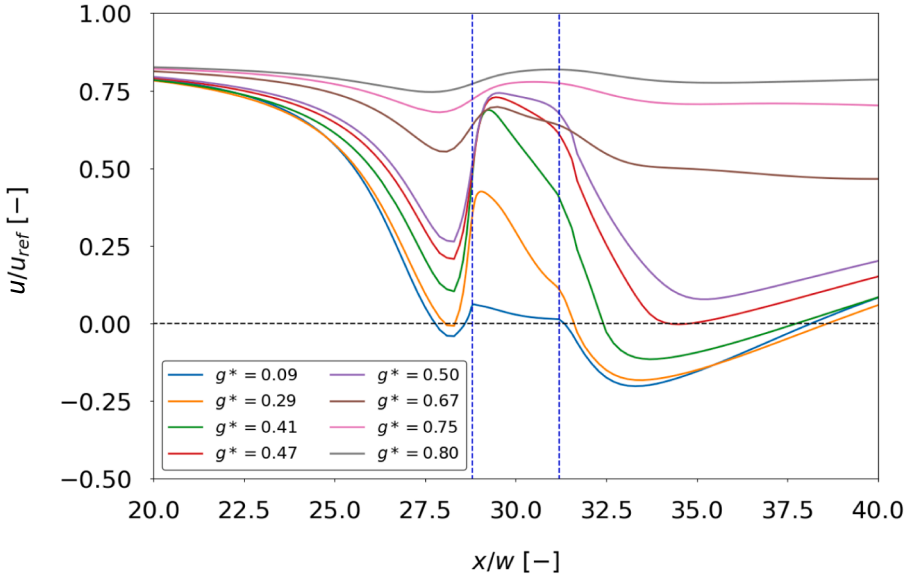

Fig. 5. Streamwise velocity, u, at $z = 0.25$ m, along the centerline of the central gap spacing between buildings for various gap ratios, g^*, and $\theta_w = 0^\circ$. The dashed blue vertical lines show the location of the buildings and hence the start and end position of the central gap. The reference wind speed is $u_{ref} = 17$ m/s. (For interpretation of the references to colour in this figure legend, the reader is referred to the web version of this article.)

streamwise velocity in front of the central gap when $g^* = 0.50$, is 6.60 times that of for the $g^* = 0.80$. Fig. 5 indicates that the streamwise velocity behind the central gap spacing for configurations with larger g^*, is significantly higher than that for configurations with smaller g^*, meaning that a higher amount of sediment transport flux towards the dune is expected just behind the central gap when the gap ratio is large.

Impact of wind incidence angle

The horizontal near-bed streamline patterns (at an elevation of $z = 0.25m$ above the bed) around a row of ten full-scale beach buildings at five different wind incidence angles, θ_w, 0°, 20°, 40°, 60°, and 80°, and a constant gap spacing of $g^* = 0.67$ are shown in Fig. 6. These figures show that the near-bed flow patterns depend on both the gap spacing between neighboring buildings and the incoming wind direction. Fig. 6a shows that in the case of buildings oriented perpendicular to the incident wind, $\theta_w = 0^\circ$, there is only one wall in each building facing the wind. Therefore, the approaching wind is split into two fractions of flow in front of the wind-facing walls, wrapping around the streamwise faces of the buildings, and creating a pair of recirculating vortices immediately behind the downwind face of the buildings. The two branches of flow are equal, and the downwind vortices are fully symmetric for buildings with large enough gap spacing. In case of obliquely oriented buildings, $\theta_w > 0^\circ$, there are two walls in each building facing the wind. The orientation of the wind-facing walls relative to the incident wind determines the location of the stagnation point at which the incoming flow is split into two branches, and the fraction of flow steered to each side of the building.

For $\theta_w = 20^\circ$, the incident wind is split at the shorter wind-facing wall of the buildings. Fig. 6b shows that a large fraction of flow is steered towards the low-pressure region just behind the downwind faces of the buildings. The deflected flows, reaching the sharp corners of the buildings are separated from the surface, and form a recirculating flow region that shows reversed flow just behind the longer downwind face of the buildings. The size of the recirculating flow region and the flow reattachment point depend on the positioning of the building in the row, gap spacing between buildings and the constraint effect due to the presence of the neighboring buildings. Therefore, the flow may reattach at the shorter downwind face of the buildings (A) like the last building in the row, the most downwind, where there is no neighboring building on its right, or at the longer downwind face of the buildings (B) like the rest of the buildings in the row. In case of flow reattachment at the longer downwind face of the buildings, the flow reaching the upper right corner of the buildings (in the top view) is again separated from the surface and creates a small rotating vortex (C). The flow is then merged with the deflected flow at the other side of the buildings to join the undisturbed flow far enough downstream of the buildings.

As the wind incidence angle increases to $\theta_w = 40^\circ$, the stagnation points move to the lower left corners of the buildings (D), and a large portion of the flow follows the longer wind-facing wall of the buildings. The reverse flow regions just behind the longer downwind face of the buildings grow for more oblique wind (E) as Fig. 6c shows. A small rotating vortex forms at some distance downstream of the shorter downwind face of the middle buildings (F), which is bounded on the outside by the deflected flow towards the longer wind-facing wall. This vortex disappears at the first building in the row, the most upwind, as the compressed flow spread out when there is no neighboring building on its left. In addition, the last building in the row does not face an obstruction in front, therefore these two vortices grow and cover the whole surface of the downwind walls, creating a separation bubble with two large asymmetric opposing vortices.

For $\theta_w = 60^\circ$, the separation point appears at the longer wind-facing wall of the buildings (G), and the flow pattern except the last building in the row, is characterized by one large vortex just behind the longer downwind face (H), and two small vortices behind the shorter downwind face of the buildings (I). For more oblique winds, the row of buildings effectively forms a single long bluff body, see Fig. 6d. Therefore, the deflected flow around the first building in the row affects the flow downstream of the rest of the buildings so that the streamlines bend slightly inwards, pushing the two small vortices behind the shorter downwind face of the buildings towards the buildings. This flow sheltering due to the most upwind building in the row is more intense for $\theta_w = 80^\circ$, in which the two small vortices almost disappear (J). As shown in Fig. 6e, the large elliptical vortex behind the longer downwind face of the buildings (K) rotate so that the longer diagonal of the vortex is along z direction rather than in x direction.

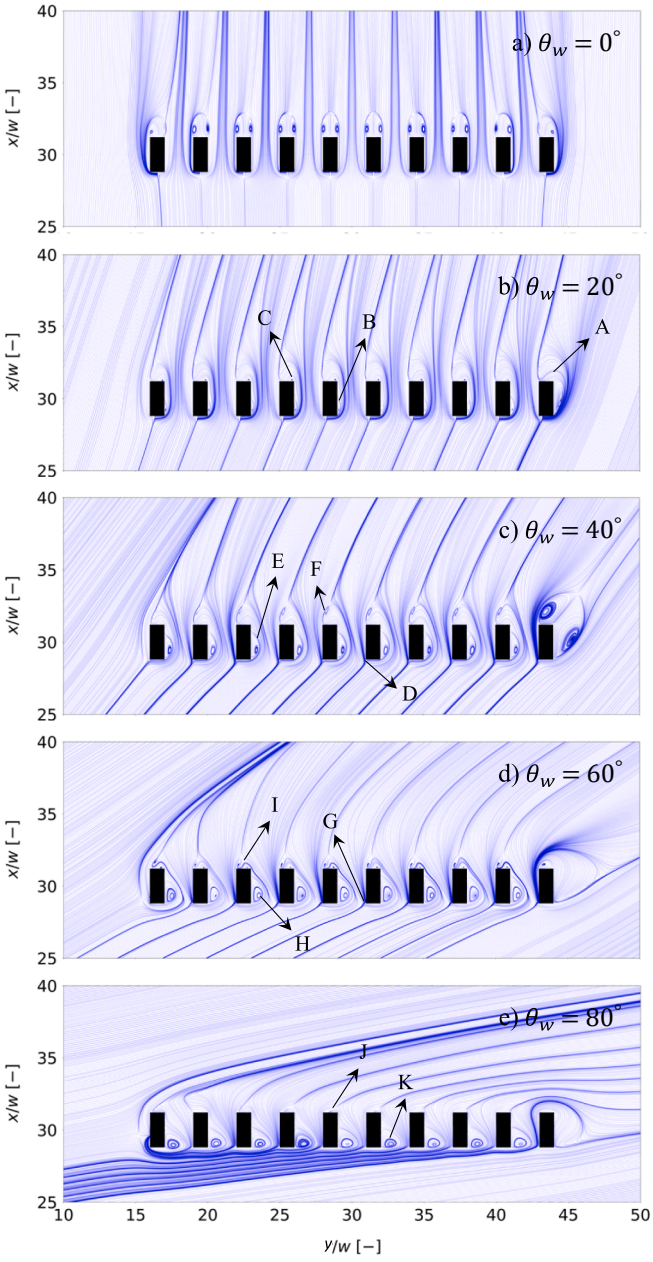

Fig. 6. Horizontal airflow patterns at a near-bed plane, $z = 0.25$ m, for $g^* = 0.67$, and the wind incidence angle, θ_w, is changed as a) 0°, b) 20°, c) 40°, d) 60°, and e) 80°.

The changes in near-bed x component of velocity along the centerline of the central gap spacing between buildings for five different wind incidence angles, and $g^* = 0.67$ are shown in Fig. 7. As shown in Fig. 7, the higher the wind incidence angle, the smaller the x component of velocity upstream of the buildings. In addition, for all wind incidence

angles, the x component of velocity decreases in front of the central gap. The difference between the highest x component of velocity far enough upstream of the buildings, and the lowest x component of velocity in front of the central gap decreases for more oblique winds. For instance, the decrease in x component of velocity from highest to the lowest value upstream of the central gap when $\theta_w = 0^\circ$ is 4.87 times greater than that of for $\theta_w = 80^\circ$.

For $\theta_w \leq 60^\circ$, the x component of velocity is then increased to an initial peak as the flow enters the central gap due to the funneling effect. In case of buildings that are placed perpendicular to the incident wind, $\theta_w = 0^\circ$, the flow decelerates and the x component of velocity gradually decreases through the remaining central gap to some distance downstream due to the flow expansion. As the incident wind becomes oblique, $\theta_w = 20^\circ, 40^\circ$ and 60°, a recirculation region forms just behind the longer downwind face of the buildings, causing a small decrease in the x component of velocity through the central gap. The incoming flow passing the central gap is constrained by this recirculation region and the deflected flow due to the presence of the neighboring building. The x component of velocity shows two local maximums because of the funneling effect between the buildings and the recirculation region added together. It should be noted that the flow pattern is slightly different for $\theta_w = 80^\circ$ compared to the other wind incidence angles greater than zero. The initial peak appears immediately in front of the central gap at $x = 28.50w$. The x component of velocity decreases slightly when the flow enters the gap, which is due to the change in the orientation of the elliptical vortex when $\theta_w = 80^\circ$ (Fig. 6e). In addition, the second peak of the x component of velocity appears earlier at $x = 30.30w$, which is located inside the central gap.

As Fig. 7 shows, the higher the wind incidence angle, the lower the initial peak. The second peak of the x component of velocity is always higher than the initial peak for $\theta_w \geq 20^\circ$, and the maximum value occurs for $\theta_w = 40^\circ$. The x component of velocity at the second peak when $\theta_w = 40^\circ$ is 3.80 times greater than that for $\theta_w = 80^\circ$. Furthermore, the x component of velocity behind the central gap spacing when $\theta_w \leq 40^\circ$ is significantly higher than the other two wind incidence angles. Therefore, the lowest duneward sediment transport flux behind the central gap is expected for the two most oblique winds. To understand which combination of the gap spacing between buildings and wind incidence angle result in the greatest amount of sediment transport towards the dunes, more quantitative justifications are needed. This will be discussed in section 3.3.3.

Wind shear stress at the bed

Impact of gap spacing

The spatial variability of the bed shear stress magnitude, $|\overrightarrow{\tau}|$, around the row of buildings with five gap ratios that generated different airflow patterns in the near-wake region, for $\theta_w = 0^\circ$ is shown in Fig. 8. The bed shear stress results can be explained by the airflow patterns and velocity shown in Figs. 4 and 5, respectively. A shadow zone with low bed shear stress develops just behind the lee face of the buildings (blue-shaded colors) as a result of flow pattern in the separation bubbles and vortices that form in the near-wake region. For smaller gap ratios, $g^* = 0.09$ and $g^* = 0.41$, another region with low bed shear stresses develops, depending on the location where the flow reattachment occurs (Fig. 8a and b). As the gap ratio increases, the bed shear stress becomes higher in the gap spacings between neighboring buildings, and immediately behind the gaps (dark, red-shaded colors). This corresponds to high velocities between the buildings (Fig. 5). For closely placed buildings, where $g^* = 0.09$, the flow passing through the gap spacings is negligible, therefore the increased bed shear stress in gaps is not apparent compared to larger gap ratios. Furthermore, two zones of high bed shear stress form on the outside of the row of buildings extending downstream. The intensity and the extension of these areas mostly depend on the gap spacing between buildings, the extent at which the air is blocked in front of the upwind faces of the buildings, is deflected towards the external buildings in the row, and being separated with high wind speeds from the sharp corners. For buildings that are placed sufficiently far apart, $g^* = 0.67$, the flow passing the gap spacings is more pronounced. Therefore, the flow blockage due to the presence of buildings, the deflected flows to the ends of the row of buildings, and the wind speed of the separated flows from corners is less substantial, producing areas with lower bed shear stresses around the buildings compared to smaller gap ratios. Similarly, the decreased bed shear stress just in front of the upwind faces of the buildings can also be explained by the flow blockage due to the presence of buildings. The closer the buildings, the lower the bed shear stress in front of the buildings.

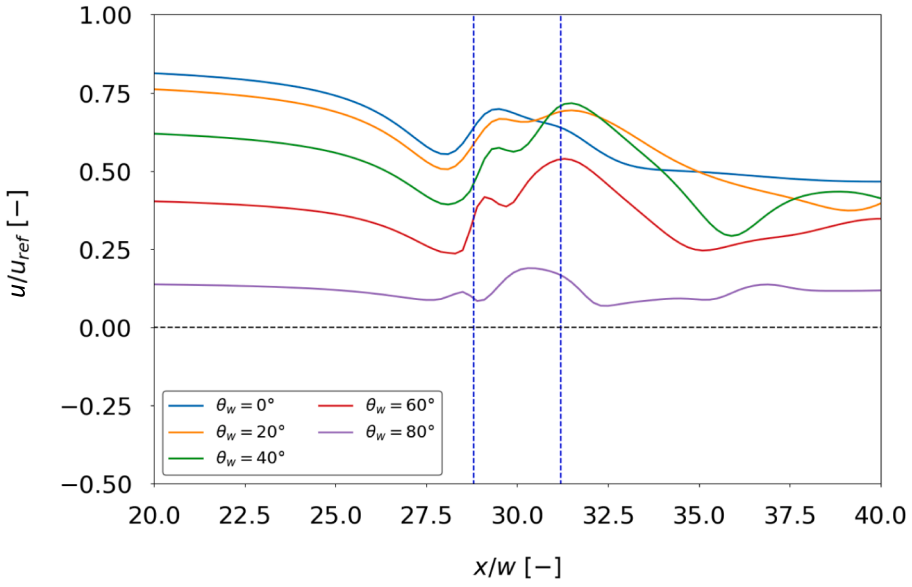

Fig. 7. X component of velocity, u, at $z = 0.25$ m, along the centerline of the central gap spacing between buildings for various wind incidence angles, θ_w, and $g^* = 0.67$. The dashed blue vertical lines show the location of the buildings and hence the start and end position of the central gap. The reference wind speed is $u_{ref} = 17$ m/s. (For interpretation of the references to colour in this figure legend, the reader is referred to the web version of this article.)

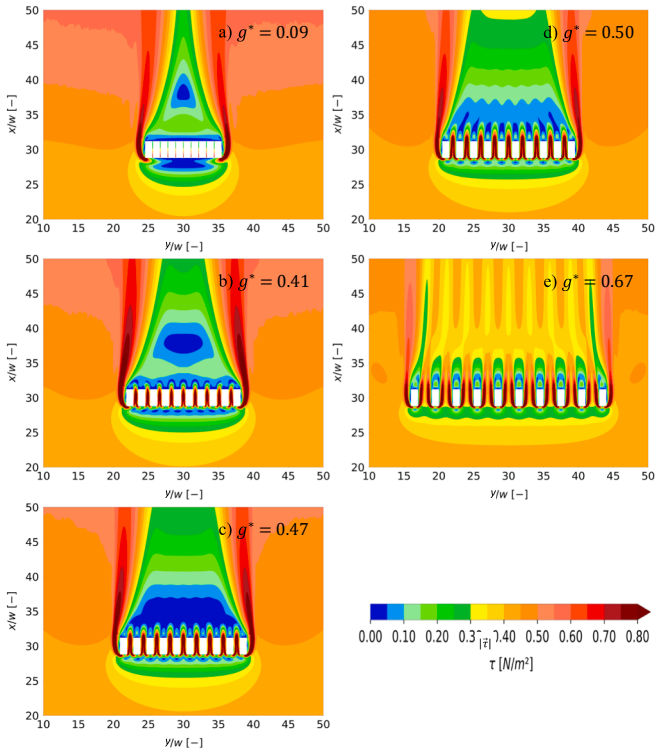

Fig. 8. Spatial distribution of bed shear stress magnitude, $|\vec{\tau}|$, when $\theta_w = 0^\circ$, and the gap ratio, g^*, is changed as a) 0.09, b) 0.41, c) 0.47, d) 0.50, and e) 0.67.

Impact of wind incidence angle

The spatial variability of the bed shear stress magnitude, $|\vec{\tau}|$, around the row of buildings under five different wind directions, for $g^* = 0.67$ is shown in Fig. 9. The bed shear stress results for different wind incidence angles show more complex patterns than with the varying gap ratios, but the overall patterns with respect to the wind-facing walls of the buildings are similar to those for the different gap spacings. For all incidence angles, the lowest bed shear stresses (blue and green-shaded colors) occur in front of the wind-facing walls of the buildings, and in the reverse flow region behind the downwind face of the buildings. For $\theta_w = 60^\circ$ and $\theta_w = 80^\circ$, the second to tenth buildings in the row are sheltered by the most upwind building (first building in the row). Therefore, the near-wake region behind buildings is characterized by a larger area of low wind shear stresses than in the other wind incidence angles. Furthermore, the increased bed shear stress (dark, red-shaded colors) in the gap spacings between buildings strongly depend on the size, location, and orientation of the circulating vortices right next to the downwind faces of the buildings (see Fig. 6). The larger separation bubble just behind the buildings confines the flow passing through the gap spacings and thus increases the funneling effect downstream of the gaps. As shown in Fig. 9b, at which $\theta_w = 20^\circ$, the areas with increased bed shear stress are narrower but longer, while Fig. 9c, at which $\theta_w = 40^\circ$, shows the wider but shorter areas with increased bed shear stress downstream of the gaps.

Sediment transport

Impact of gap spacing

The duneward sediment transport flux, q_c, distribution at the bed of the computational domain around a row of ten full-scale beach buildings with five different gap ratios for $\theta_w = 0^\circ$ is shown in Fig. 10. Results for each examined gap ratio show that the duneward sediment transport flux is greatest (red-shaded colors) through the gap spacings between buildings, and around the both ends of the row of buildings towards downstream. The lowest values of the duneward sediment transport flux occur in front of the windward face of the buildings, and behind the buildings, especially in the near-wake region in the wind shadow of buildings. It should be noted that the zero-duneward sediment transport flux is associated with the alongshore local wind directions, and the locations where the wind shear velocity, $\vec{u_*}$, is less than threshold shear velocity, u_{*th}. Furthermore, the negative sediment transport flux occurs within the separation bubble just behind the buildings or in front of buildings, where the flow direction is in opposite direction relative to the prevailing wind direction.

Impact of wind incidence angle

The duneward sediment transport flux, q_c, distribution at the bed of the computational domain around a row of ten full-scale beach buildings under five different wind directions, for $g^* = 0.67$ is shown in Fig. 11. Results show that the duneward sediment transport flux is lowest for the two most oblique wind directions, $\theta_w = 60^\circ$ and $\theta_w = 80^\circ$. This means that the sediment particles are likely to be transported laterally as the prevailing wind direction becomes more alongshore rather than cross-shore. Furthermore, for $g^* = 0.67$, a slightly oblique wind direction, where $\theta_w = 20^\circ$, causes sediment transport to continue longer downstream. This might increase the chance that the sediments from the beach reach the dune toe and be deposited somewhere in front of the dune or to maintain transport and being deposited further over the dune.

Comparison between different configurations

In the two previous sections, we focused on the systematic study of how the gap spacing between buildings and the dominant wind direction affect the spatial structure of potential sediment transport towards the dunes. However, to be able to systematically investigate the combined impact of gap spacing and the wind direction, we need to quantify the sediment transport in the downwind direction. In order to make an explicit comparison between 80 tested simulations, consisting of 16 different gap spacings, each tested for five different wind directions, a method is needed to find a single representative number for duneward sediment transport in each simulation, which can be compared between different simulations. For this purpose, two lines in the alongshore direction, z, are defined downstream of the row of buildings. Fig. 12 displays that line 1 and line 2 are located 5 m, and 70 m downstream of the lee face of the buildings, respectively. These two lines were selected, because the beach buildings are mostly placed at 5 −10 m distance from the dune toe. Line 1 is thus representative of a typical location of a dune foot, whereas Line 2 represents a location much further downstream, i.e. somewhere well inside the dunes (but without actually modelling the dunes themselves). The average duneward sediment transport flux in x direction is then computed over these lines for all simulations with different combinations of gap spacing and wind direction. In order to compare the net effect of buildings on duneward sediment transport, the average transport flux along line 1 and line 2 in an empty domain without buildings, $q_{c_{ref}}$, are subtracted from the average transport flux in the domain including buildings, q_c. The results are shown in Fig. 13, where each point corresponds to an individual simulation.

The blue shaded colors in Fig. 13 show $q_c < q_{c_{ref}}$, indicate that the duneward sediment transport passing a given line in the presence of buildings is less than when there is no building at the beach. Similarly, the red shaded colors, $q_c > q_{c_{ref}}$, denote that the duneward sediment transport passing that line increases when the buildings are placed at the beach compared to the empty beach. In case of closely spaced beach buildings, $g^* < 0.67$, the buildings contribution on duneward sediment transport passing line 1 is small and mostly negative (see Fig. 13a). In this situation, the highest positive effect of buildings on duneward sediment transport occurs when $\theta_w = 20^\circ$. As the gap ratio increases, $g^* \geq 0.67$, the duneward sediment transport in the presence of buildings compared to the situation without buildings, is decreased for 0° and 80° winds, while it is enhanced for other wind directions. The highest

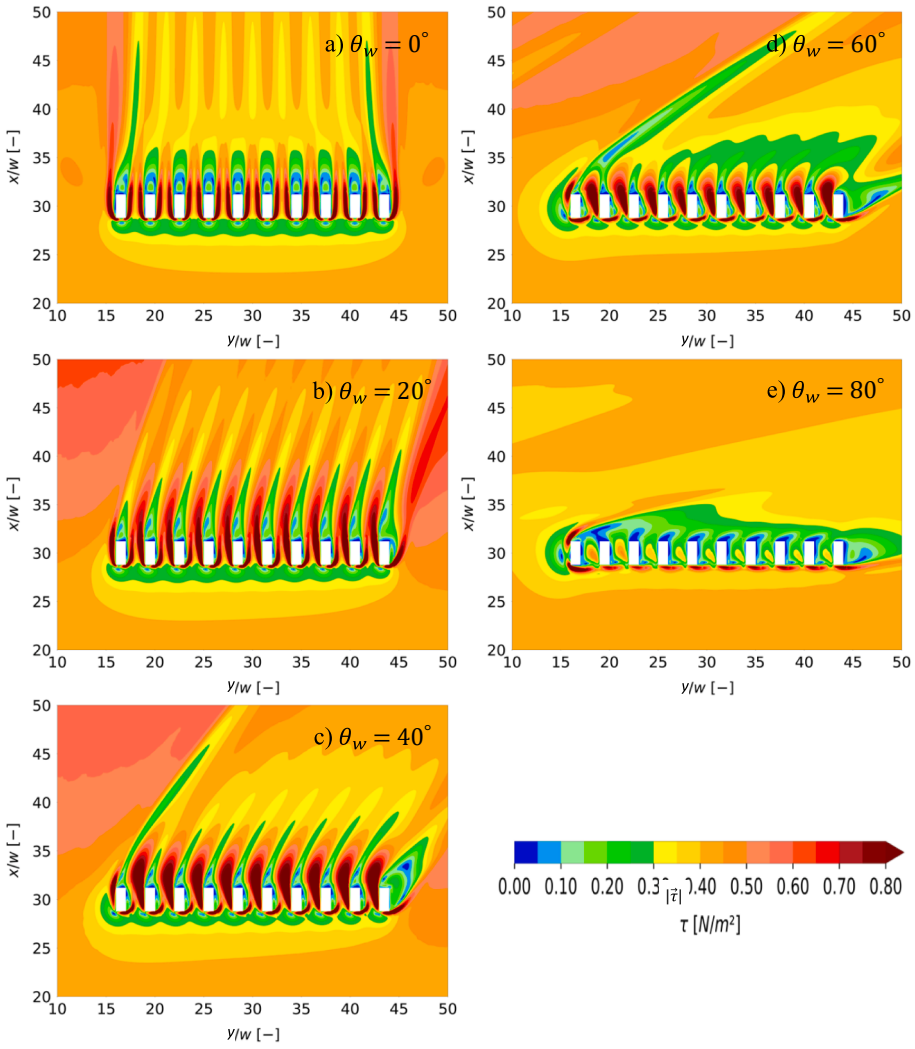

Fig. 9. Spatial distribution of bed shear stress magnitude, $|\vec{\tau}|$, when $g^* = 0.67$, and the wind incidence angle, θ_w, is changed as a) 0°, b) 20°, c) 40°, d) 60°, and e) 80°.

enhanced duneward sediment transport due to the buildings occurs when $\theta_w = 40^\circ$ and $\theta_w = 60^\circ$.

Further downstream of the row of buildings, the buildings contribution on duneward sediment transport passing line 2 is positive in almost all combinations of the gap spacings and the wind directions (see Fig. 13b). Results show that the highest enhanced sediment transport towards the dunes due to the presence of buildings occurs for 20° winds. Furthermore, the difference between the duneward sediment flux leaving line 2 in the situation with and without buildings is higher for closely spaced buildings compared to when buildings are far apart from each other.

The exact values of the average duneward sediment transport flux due to the presence of buildings, $q_c - q_{c_{ref}}$, for 80 tested simulations computed along line 1 and line 2, shown in Fig. 13, are presented in Table 3 and Table 4, respectively, in the appendix.

Initial changes in bed elevation

The Exner equation, Eq. [5], is used to compute the initial bed evolution on the basis of mass continuity. This approach relates the temporal changes in bed elevation, $\partial z_b/\partial t$, to divergence or convergence in sediment transport flux, $\vec{\nabla}\cdot\vec{q}$. Fig. 14 presents the initial erosion and deposition patterns derived from the Exner equation for three different gap ratios. To validate the model results, the initial bed level change computed by the numerical model are qualitatively compared with the deposition pattern observed around a row of three scaled beach buildings shown in Fig. 15. The experiments were conducted by Poppema et al. (2022) to investigate the impact of gap spacing between scaled beach buildings, and the buildings orientation at the beach on the sediment deposition pattern that develop around buildings. Although there are some differences between the numerical and experimental model setup, the deposition patterns are comparable. The differences between field and model include the number of tested buildings in the row, buildings dimension, wind speed, multi-directional wind at the beach, supply-limited conditions at the beach i.e. moisture, existing ripples, and other roughness elements such as shells at the beach.

As shown in both Fig. 14a and 15a, in case of closely spaced buildings (beside each other at the field experiment), the row of buildings act more like a very wide building where sand deposited in the low-speed region in front of the upwind face of the large building and formed a continuous horseshoe-shaped deposition area. This upwind deposition indents in both numerical model and experiment as the gap ratio increases to 0.50 (see the black ovals in Fig. 14b and 15b). Furthermore, results show that short, triangulated deposition tails form just behind the gap spacing between two neighboring buildings. Based on the numerical results shown in Fig. 14c, for larger gap ratio, 0.67, these inner deposition tails split up into two longer and narrower deposition tails that wrap around the buildings and continue to some extent downstream. Fig. 15c shows a

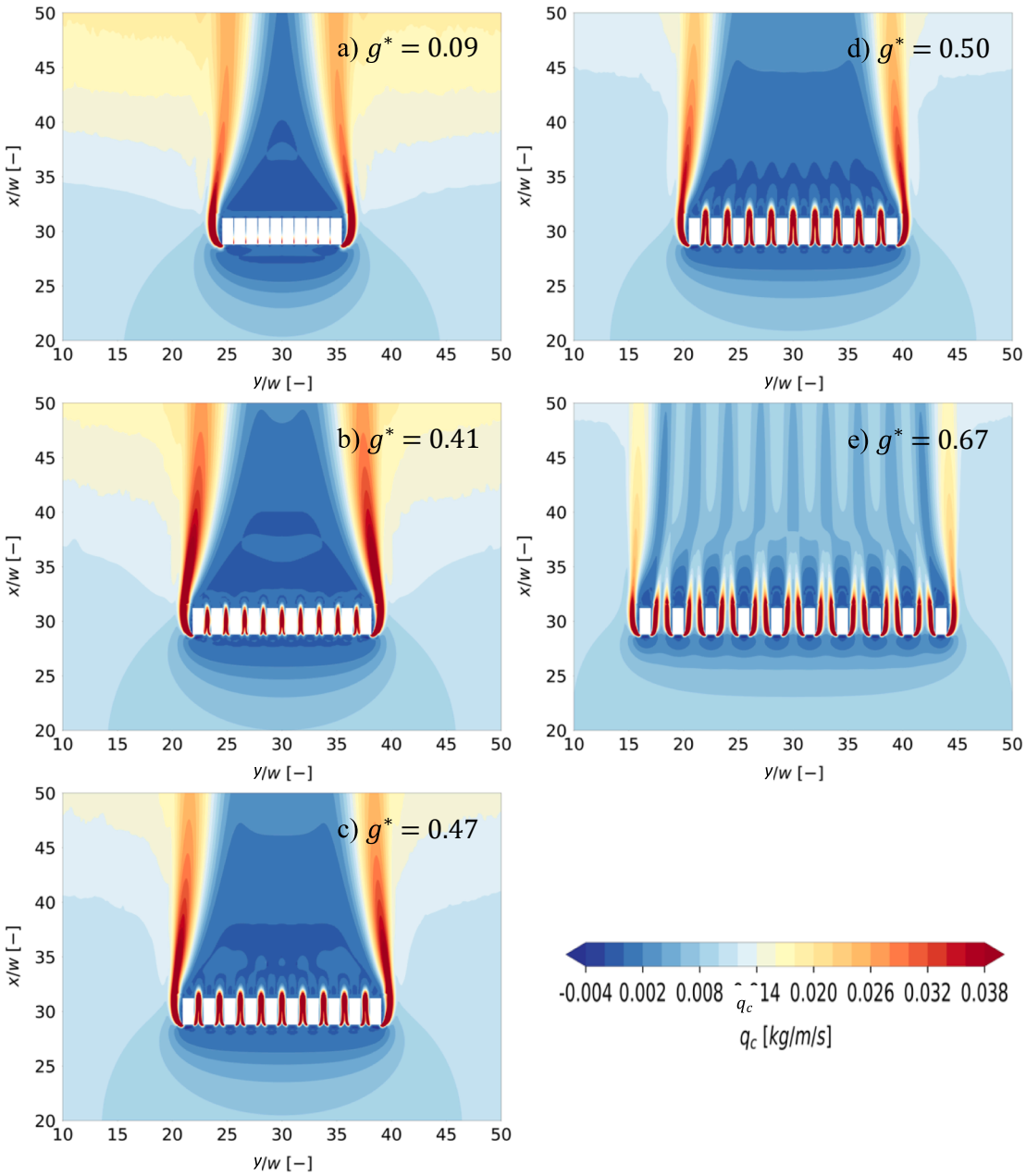

Fig. 10. Spatial distribution of duneward sediment transport flux, q_c, when $\theta_w = 0^\circ$, and the gap ratio, g^*, is changed as a) 0.09, b) 0.41, c) 0.47, d) 0.50, and e) 0.67.

different shape of the inner deposition tails in the field. This difference might be because of the temporal changes in the wind direction at the beach. As the wind swings between two bounding directions, two adjacent tails gradually merge, and form a single deposition tail downstream of the gaps. The darker red colors in Fig. 14c show that the two outer deposition tails tend to become shorter as the size of the gap increases. In addition, the upwind depositions form at a closer distance relative to the upwind faces of the buildings, and their peaks become almost separate from neighboring peaks.

Discussion

The aerodynamic behavior of wind flow around adjacent beach buildings is an interesting coastal engineering problem, because of the influence that these complex flows might have on the sediment supply from the beach to the dunes. Also, the sediments might accumulate around the buildings and cause failure of the buildings structure. In addition, the arrangement of the structures can influence the sand transport directing it towards the toe or top of the dunes downstream of the buildings. The latter helps the natural flood defense functioning of the dunes. The airflow patterns that developed in the near-wake region behind the row of buildings in this study are consistent with those observed in wind-tunnel experiments of previous studies.

For example, the observed variations in flow patterns for different tested gap ratios in the wind-tunnel experiments conducted by Luo et al. (2014) are comparable with our findings in Fig. 4. Although we examined ten full-scale longitudinal buildings compared to two wide small-scale buildings tested in Luo et al. (2014), the flow mechanisms proposed by them are still recognizable in our model results. We tried a wider range of gap ratios, $g^* = 0.09 - 0.80$, compared to $g^* = 0.09 - 0.44$ of Luo et al. (2014), and observed that almost all switches in flow behavior when the gap size increases occur at a larger gap ratio than those suggested by Luo et al. (2014). Comparing their flow classification based on the mean streamlines in the near-wake

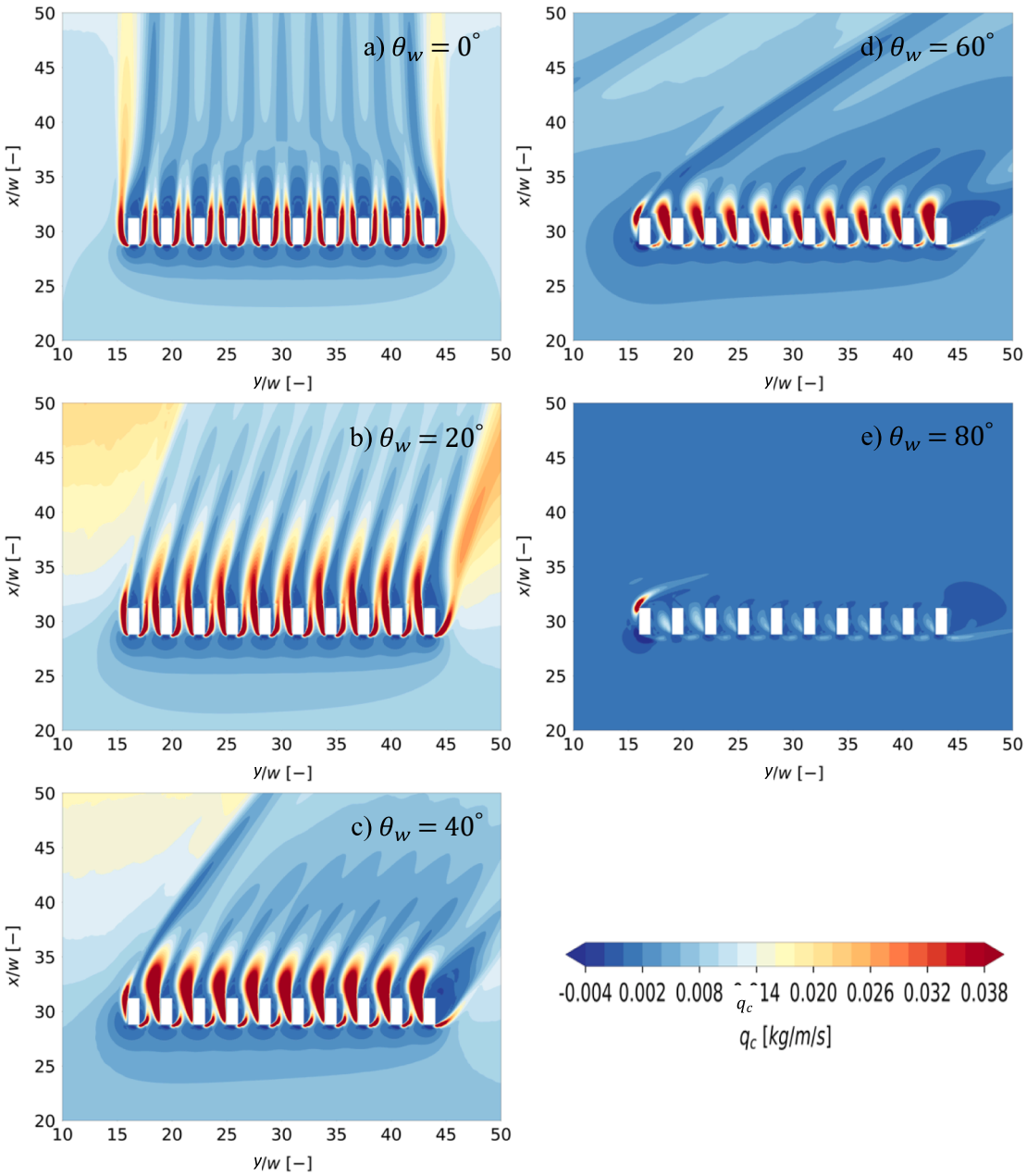

Fig. 11. Spatial distribution of duneward (the × component of) sediment transport flux, q_c, when $g^* = 0.67$, and the wind incidence angle, θ_w, is changed as a) 0°, b) 20°, c) 40°, d) 60°, and e) 80°.

region, with the streamlines in our steady-state simulations (see Fig. 4), we observed the single-vortex flow pattern at $g^* = 0.09$, gap-enveloped flow pattern at $g^* = 0.41$, wake-interference flow pattern at $g^* = 0.47$, and at $g^* \geq 0.50$ the streamlines of our simulations seem to correspond well with their time-averaged coupled vortex-street flow pattern. Furthermore, wind-tunnel results for the coupled vortex-street mode, i.e. $g^* = 0.44$ in Luo et al. (2014), show almost symmetric counter-rotating vortices just behind the lee face of both buildings. However, the streamlines downstream of the reattachment point of flow is not fully parallel with the dominant wind direction. Therefore, the gap ratio of 0.44 appears to be the critical gap spacing below which the airflow patterns around buildings are affected by the neighboring building. Our numerical model results showed almost independent flow patterns, when $g^* \geq 0.67$ (see Fig. 4e). At first glance, we could attribute this lag in flow patterns to the scale at which the buildings are modelled experimentally and numerically. The field experiments around scaled buildings at the beach, performed by Poppema et al. (2022), however showed the same critical gap ratio, $g^* = 0.67 - 0.75$, as observed for our numerical model results. This is likely because even though the geometrical scales in the numerical model and field experiments are different, the frontal width-to-height aspect ratio, w/h, in both our simulations and scaled models at the beach is similar, $w/h = 1$.

The difference in the length of the area with low bed shear stress (green-shaded colors in Fig. 9b, c and d) behind the leading building in the row can be explained by the flow patterns shown in Fig. 6. For $\theta_w = 20^\circ$, the short face of the buildings is the windward face. The flow streamlines in the wake region downwind of the buildings are almost parallel to each other (Fig. 6b). As the wind incidence angle increases to $\theta_w = 40^\circ$, the wind is separated at approximately the lower left corner of the buildings. The results showed that the downwind flow behind the reattachment point of the leading building is slightly inclined compared to the direction of the downwind streamlines behind the rest of the

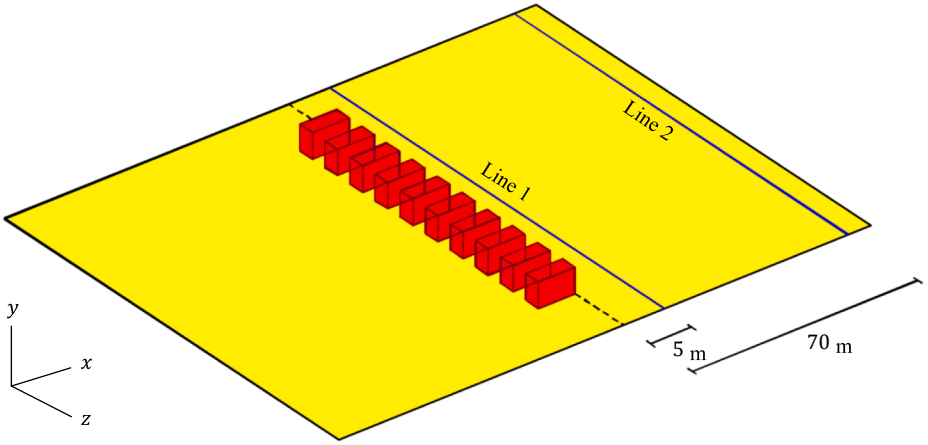

Fig. 12. The location of the two lines downstream of the buildings, that the average duneward sediment transport flux is computed along.

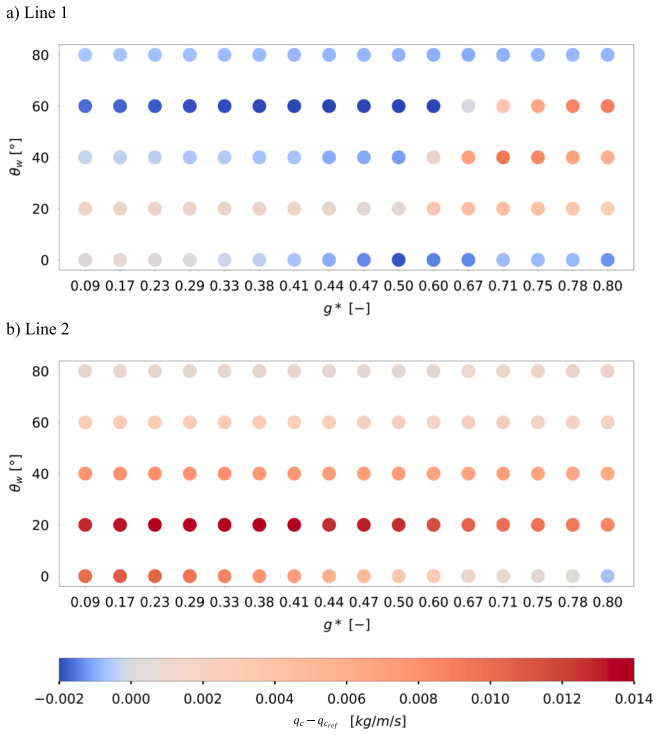

Fig. 13. Comparison of the net impact of buildings on average duneward sediment transport flux, $q_c - q_{c_{ref}}$, between 80 different combinations of gap ratio, g^*, and the wind incidence angle, θ_w, computed along a) line 1, and b) line 2, which are located at 5 m and 70 m downstream of the row of buildings (shown in Fig. 12), respectively.

buildings in the row (Fig. 6c). For more oblique wind direction, $\theta_w = 60^\circ$, the long face of the buildings is facing the wind. The buildings tend to act more like a very long building against the wind. Therefore, the vortices behind the buildings are smaller, the reattachment points downwind of the buildings get closer to the lee face of the buildings and the downwind streamlines become curved. It seems that the deflected flow around the leading building pushes the flow behind the other buildings in the row (Fig. 6d). The wind-induced friction behind the leading building depends on the extent to which the flow momentum is being pushed by the deflected flow around the leading building. This could be an explanation for the various length of the region with low bed shear stress behind the leading building when buildings are exposed to different wind incidence angles.

Comparisons between the bed level changes based on the numerical model and field experiments show generally good agreement. However, there are some differences between numerically predicted erosion and deposition patterns and those observed at the beach. There are several reasons that can be put forth to explain the differences. The first reason is that the scale of tested buildings and the number of buildings placed besides each other in the numerical model differs from those used in the field study by Poppema et al. (2022). In the field study, three scaled beach buildings with the length, width, and height of $1 \times 0.5 \times 0.5$ m were placed at the beach, while considering the same frontal aspect ratio, we tested ten full-scale buildings of size $6 \times 2.5 \times 2.5$ m. Secondly, the actual wind field at the beach is unsteady, with the wind direction and speed show strong variations over time, whereas in the model the wind speed and direction are not varying. Although, the one-day experiments by Poppema et al. (2022) limits the variations in wind condition, the variation could potentially influence the shape and size of the bed topography patterns. Thirdly, we considered the transport-limited (i.e., not supply-limited) condition in our model, such that the bed of the numerical domain can unlimitedly provide sediment particles. The bed in the model is fully dry and flat, and consists of non-cohesive and uniformly-graded particles. However, there are some adverse impacts at the real beach bed that lead to the supply-limited condition, in which the capability of the bed to supply sediment particles becomes limited. Conditions that limit the sediment availability at the beach include bed moisture content, vegetation, ripples, sediments sorting, slope, and beach armoring (Delgado-Fernandez, 2010; Nolet et al., 2014; Silva et al., 2018; Hoonhout and de Vries, 2019). This might be the reason for the differences observed in the deposition region around scaled beach buildings, and more horse-shoe shaped deposition in the numerical model. Finally, we assumed a uniform aerodynamic roughness length, z_0, for the bed surface of the numerical model domain, but uniformity is not likely in reality where grains of different sizes occur and small-scale bedforms will also influence the roughness. Next to this the bed level changes derived from Exner equation, are the initial patterns developed at a flat beach where the local morphological feedback has not been taken into account. The erosion and deposition patterns developed around buildings change the beach topography, which might locally influence the wind speed and direction, and in turn alter the wind-induced shear stresses. Furthermore, the actual beach bed consists of spatially different roughness. This is due to the existence of shells, vegetation, and sand grains with different sizes. Although the above-mentioned differences between the actual beach situations and our model assumptions exist, the comparisons between the field observations and our numerical model results are in good agreement.

Table 3
Net buildings-induced average duneward sediment transport flux, $q_c - q_{c_{ref}}$ [$\times 10^{-4}$ kg/m/s], along line 1 for 80 different combinations of gap ratio, g^*, and the wind incidence angle, θ_w, corresponding to Fig. 13a.

g^* [-] / θ_w [°]	0.09	0.17	0.23	0.29	0.33	0.37	0.41	0.44
0	2.36	4.46	2.49	−0.13	−2.04	−3.68	−5.64	−9.91
20	13.04	13.68	16.20	13.51	16.36	15.12	14.73	9.47
40	−2.81	−3.59	−3.78	−5.89	−5.01	−6.79	−6.63	−9.91
60	−16.15	−17.18	−17.96	−18.83	−19.28	−19.75	−20.16	−20.70
80	−6.10	−6.50	−6.88	−7.26	−7.59	−7.87	−8.18	−8.49
g^* [-]	0.47	0.50	0.60	0.67	0.71	0.75	0.78	0.80
θ_w [°]								
0	−13.45	−18.50	−14.17	−13.85	−7.40	−7.58	−7.90	−12.78
20	7.99	4.94	33.28	41.79	41.64	40.86	35.06	26.94
40	−10.12	−11.85	12.51	68.07	93.78	83.64	68.77	55.92
60	−20.94	−21.66	−21.26	−0.84	32.05	64.34	84.81	90.07
80	−8.60	−8.81	−9.36	−9.60	−9.34	−8.66	−8.25	−8.69

Table 4
Net buildings-induced average duneward sediment transport flux, $q_c - q_{c_{ref}}$ [$\times 10^{-4}$ kg/m/s], along line 2 for 80 different combinations of gap ratio, g^*, and the wind incidence angle, θ_w, corresponding to Fig. 13b.

g^* [-] / θ_w [°]	0.09	0.17	0.23	0.29	0.33	0.37	0.41	0.44
0	100.57	106.33	101.86	94.79	86.67	77.29	70.83	55.24
20	127.86	131.74	138.81	133.85	142.54	137.17	137.25	126.64
40	77.80	79.14	80.90	77.21	79.78	75.08	74.91	69.14
60	27.84	27.73	28.45	27.64	27.93	27.01	26.16	24.09
80	9.09	9.13	9.10	9.10	9.30	9.20	8.88	8.27
g^* [-]	0.47	0.50	0.60	0.67	0.71	0.75	0.78	0.80
θ_w [°]								
0	46.64	32.15	28.68	15.38	11.20	4.44	1.40	−6.90
20	130.17	125.59	114.78	103.09	98.37	95.82	93.17	86.06
40	70.74	69.10	67.08	66.87	69.17	66.23	64.51	61.93
60	23.07	21.42	18.13	20.02	20.18	19.15	19.26	19.25
80	8.73	8.53	8.63	10.39	11.38	12.24	12.50	12.51

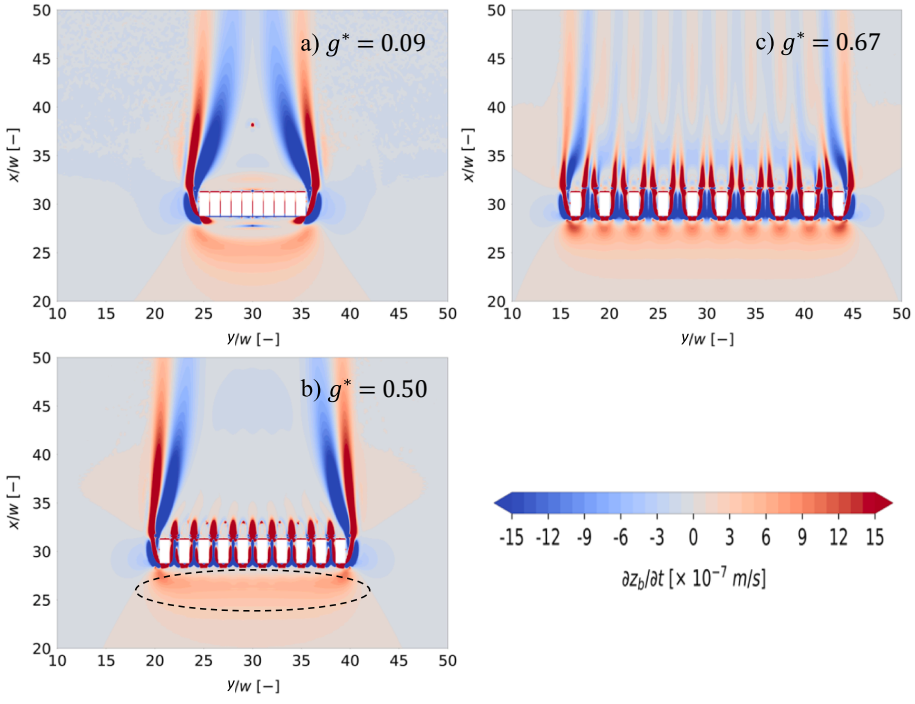

Fig. 14. Initial erosion and deposition patterns, $\partial z_b/\partial t$, for $\theta_w = 0^\circ$, and the gap ratio, g^*, is changed as a) 0.09, b) 0.50, and c) 0.67.

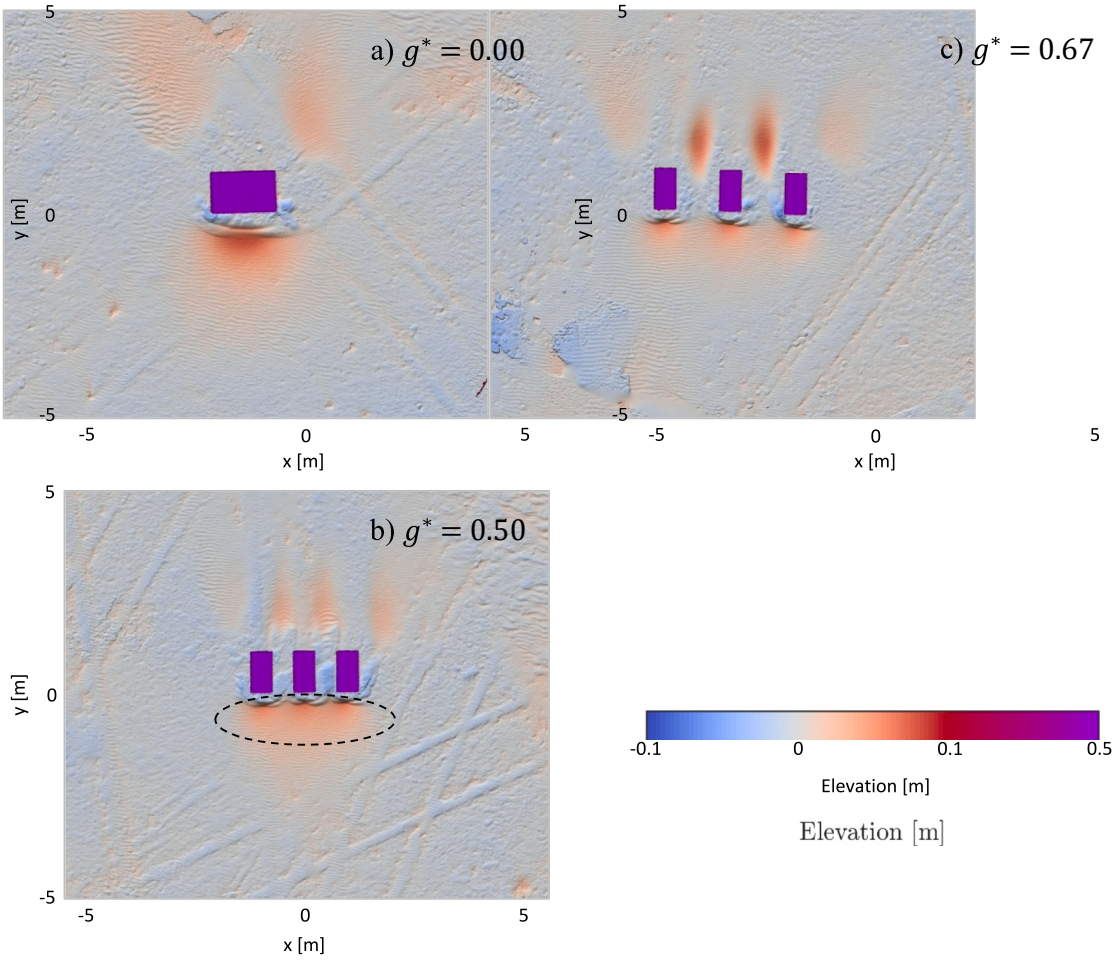

Fig. 15. Field measurements by Poppema et al. (2022) of bed elevation around a row of scaled beach buildings, when $\theta_w = 0^{\circ}$, and the gap ratio, g^*, is changed as a) 0, b) 0.50, and c) 0.67. Figures were derived using a digital elevation model, where the elevations are computed relative to a fitted linear surface (see Poppema et al., 2022).

Conclusion

This study aims to understand how the airflow characteristics and wind-induced bed shear stress, which directly affect the sediment transport and bed topography, are influenced by the positioning of buildings at the beach. This research focused on a row of ten buildings having systematic changes in the gap spacing between two neighboring buildings, and the incident wind direction relative to the buildings.

Our findings showed that the gap ratio, g^*, between neighboring buildings is a key parameter in flow behavior and resulting bed shear stress in the vicinity of buildings, which determines the sediment transport and bed elevation around and in between buildings. We found that the flow through the gap between buildings placed very close to each other, $g^* = 0.09$, is limited. Therefore, the increased bed shear stress through the gaps is not apparent, and the results showed no deposition in the lee of the gaps. The closely-spaced buildings mainly act as a single building, creating a continuous large horseshoe-shaped deposition region starting at some distance upstream of the upwind faces of the buildings. Furthermore, two deposition tails develop around the corner buildings in the row and extend downstream of the buildings.

The flow through the larger gap spacings, i.e. $g^* > 0.50$, significantly increases due to funneling effects, while the wind speed begins to decrease afterwards. This flow deceleration causes some of the sediment in transport to be deposited as so-called sand drift in the lee of the gaps. In addition, our findings showed that the upwind deposition becomes indented and develops at a closer distance relative to the upwind faces of buildings for larger gap ratios. For $g^* \geq 0.67$, both flow patterns and initial erosion and deposition patterns develop mostly independent from neighboring buildings. The jet flows passing through gaps between buildings remain parallel to the incident wind, and the separated flows from upwind edges of each building create a pair of opposing vortices just behind the lee face of buildings without interfering with the airflow around adjacent buildings. The upwind deposition peaks become separated from each other, and the length of the outer deposition tails decreases and becomes almost equal to inner deposition tails. It should be noted that the sand drifts no longer develop downstream of the gaps, and instead two deposition tails wrap around individual buildings and extend farther downstream than sand drifts in $g^* < 0.67$ conditions.

Another key factor that largely affects the size and the location at which the vortices form around buildings, is the wind incidence angle. Depending on the dominant wind direction, the separation bubble downwind buildings might locate behind the smaller face of the buildings or in between two neighboring buildings and close to the longer face. The latter would obstruct the incoming wind from entering the gap spacing and moving downstream towards the dunes. On the other hand, the wind entering the narrow space bounded on one side by the outer edges of the recirculation vortex downwind of the building, and on another side by the diverted flow from the sharp edge of the next building, experiences a funneling effect. Upon leaving this narrow gap, the flow expands and decelerates downstream, leading to the formation of larger sand drifts. It is noteworthy that these flow behaviors strongly depend on the gap spacing between buildings and the dimension of the

buildings. Furthermore, we found that for $\theta_w \geq 60^{\circ}$, the streamlines behind the flow reattachment point downstream of the second to the last building, are influenced by the diverted flow from the sharp edges of the most upwind building in the row. This leads to slightly bent streamlines directly behind the reattachment point instead of straight streamlines parallel with the dominant wind direction. As wind direction increases to $\theta_w = 80^{\circ}$, the flow pattern around buildings is mostly similar to those developed around a very long building, when the wind is almost perpendicular to the shorter face of the long building. Therefore, results show that the orientation of vortices form just behind the downwind face of buildings change for 90 degree compared to less oblique winds (the longer diagonal of the elliptical vortices in x direction).

To determine the combined impact of gap spacing and wind direction on sediment transport rate towards the dunes behind the row of buildings, we determined the average of transport flux along two different lines located at 5 m and 70 m downstream of the buildings. We have checked other distances as well, and have seen that 5 m and 70 m are representative of a typical location of a dune foot and a location well inside the dunes, respectively. The average sediment transport along these lines was used as the representative numbers for duneward sediment transport that could be compared between 80 different combinations of the gap ratio and wind direction. This approach is useful for coastal designers to compare complex building configurations and find an optimal building positioning at the beach to minimize the dunes erosion or enhance the dunes growth. We found that, different than our expectations, buildings might have positive effects on the duneward sediment transport. Complex flow patterns develop as a result of the presence of buildings at the beach, which could steer more sediments to the dunes. Results showed the maximum duneward sediment transport across a line 5 m downwind of the buildings occurs when $g^* = 0.71$ and $\theta_w = 40^{\circ}$; while the maximum along 70 m downwind of the buildings would occur for the combination of $g^* = 0.33$ and $\theta_w = 20^{\circ}$. Therefore, these findings motivate further research whether an optimum distance exists between a row of beach buildings and the dune foot so that it maximally promotes the sediment transport from the beach to the dunes under natural (variable) wind conditions.

Declaration of Competing Interest

The authors declare the following financial interests/personal relationships which may be considered as potential competing interests: Kathelijne Wijnberg reports financial support was provided by Netherlands Organisation for Scientific Research (NWO). Kathelijne Wijnberg reports financial support was provided by Rijkswaterstaat (RWS). Kathelijne Wijnberg reports financial support was provided by Hoogheemraadscap Hollands Noorderkwartier (HHNK). Paran Pourteimouri reports a relationship with J.M. Burgerscentrum that includes: travel reimbursement.

Data availability

No data was used for the research described in the article.

Acknowledgments

This research is part of the ShoreScape project, which is a joint research project of the University of Twente and Delft University of Technology. ShoreScape focuses on sustainable co-evolution of the natural and built environment along sandy shores. This research was funded by Netherlands Organisation for Scientific Research (NWO) (contract number ALWTW.2016.036) and co-funded by Rijkswaterstaat (RWS) and Hoogheemraadscap Hollands Noorderkwartier (HHNK).

References

Bagnold, R.A., 1937. The transport of sand by wind. Geogr. J. 89 (5), 409–438.
Bagnold, R.A., 1941. The Physics of Blown Sand and Desert Dunes. Metheun, London.
Bauer, B.O., Davidson-Arnott, R.G., 2003. A general framework for modeling sediment supply to coastal dunes including wind angle, beach geometry, and fetch effects. Geomorphology 49 (1–2), 89–108.
Bauer, B.O., Hesp, P.A., Walker, I.J., Davidson-Arnott, R.G., 2015. Sediment transport (dis) continuity across a beach–dune profile during an offshore wind event. Geomorphology 245, 135–148.
Becker, S., Lienhart, H., Durst, F., 2002. Flow around three-dimensional obstacles in boundary layers. J. Wind Eng. Ind. Aerodyn. 90 (4–5), 265–279.
Beranek, W.J., 1984. Wind environment around single buildings of rectangular shape. Heron 29 (1), 4–31.
Blocken, B., Stathopoulos, T., Carmeliet, J., 2007. CFD simulation of the atmospheric boundary layer: wall function problems. Atmos. Environ. 41 (2), 238–252.
Chou, J.H., Chao, S.Y., 2000. Branching of a horseshoe vortex around surface-mounted rectangular cylinders. Exp. Fluids 28 (5), 394–402.
Cooke, R.U., Warren, A., Goudie, A.S., 1993. Desert Geomorphology. CRC Press.
Delgado-Fernandez, I., 2010. A review of the application of the fetch effect to modelling sand supply to coastal foredunes. Aeolian Res. 2 (2–3), 61–70.
Delgado-Fernandez, I., Davidson-Arnott, R., 2011. Meso-scale aeolian sediment input to coastal dunes: The nature of aeolian transport events. Geomorphology 126 (1–2), 217–232.
Gao, Y., Chow, W.K., 2005. Numerical studies on air flow around a cube. J. Wind Eng. Ind. Aerodyn. 93 (2), 115–135.
Hoonhout, B., de Vries, S., 2019. Simulating spatiotemporal aeolian sediment supply at a mega nourishment. Coast. Eng. 145, 21–35.
Horikawa, K., Hotta, S., Kubota, S., Katori, S., 1983. On the sand transport rate by wind on a beach. Coastal Eng. Japan 26 (1), 101–120.
Hsu, S.A., 1971. Wind stress criteria in eolian sand transport. J. Geophys. Res. 76 (36), 8684–8686.
Hunt, J.C.R., Abell, C.J., Peterka, J.A., Woo, H., 1978. Kinematical studies of the flows around free or surface-mounted obstacles; applying topology to flow visualization. J. Fluid Mech. 86 (1), 179–200.
Iaccarino, G., Ooi, A., Durbin, P.A., Behnia, M., 2003. Reynolds averaged simulation of unsteady separated flow. Int. J. Heat Fluid Flow 24 (2), 147–156.
Iversen, J. D., Wang, W. P., Rasmussen, K. R., Mikkelsen, H. E., & Leach, R. N. (1991). Roughness element effect on local and universal saltation transport. In Aeolian Grain Transport (pp. 65-75). Springer, Vienna.
Jackson, N.L., Nordstrom, K.F., 2011. Aeolian sediment transport and landforms in managed coastal systems: a review. Aeolian Res. 3 (2), 181–196.
Kawamura, R., 1951. Study on sand movement by wind. Rept. Inst. Sci. Technol. 5, 95–112.
Lakehal, D., Rodi, W., 1997. Calculation of the flow past a surface-mounted cube with two-layer turbulence models. J. Wind Eng. Ind. Aerodyn. 67, 65–78.
K. Lettau, H. Lettau, Experimental and micrometeorological field studies of dune migration. In: Lettau, K., Lettau, H. (Eds.), Exploring the World's Driest Climate. University Wisconsin-Madison, IES Report 101, 1977, pp. 110–147.
Livingstone, I., Warren, A., 1996. Aeolian Geomorphology: An Introduction. Addison Wesley Longman, England, p. 211.
Luo, W., Dong, Z., Qian, G., Lu, J., 2012. Wind tunnel simulation of the three-dimensional airflow patterns behind cuboid obstacles at different angles of wind incidence, and their significance for the formation of sand shadows. Geomorphology 139, 258–270.
Luo, W., Dong, Z., Qian, G., Lu, J., 2014. Near-wake flow patterns in the lee of adjacent obstacles and their implications for the formation of sand drifts: a wind tunnel simulation of the effects of gap spacing. Geomorphology 213, 190–200.
Luo, W., Lu, J., Qian, G., Dong, Z., 2016. Influence of the gap ratio on variations in the surface shear stress and on sand accumulation in the lee of two side-by-side obstacles. Environ. Earth Sci. 75 (9), 1–12.
Martinuzzi, R., Tropea, C., 1993. The flow around surface-mounted, prismatic obstacles placed in a fully developed channel flow (data bank contribution).
Nickling, W.G., Neuman, C.M., 2009. Aeolian sediment transport. In: Parsons, A.J., Abrahams, A.D. (Eds.), Geomorphology of Desert Environments. Springer Netherlands, Dordrecht, pp. 517–555.
Nolet, C., Poortinga, A., Roosjen, P., Bartholomeus, H., Ruessink, G., Magar, V., 2014. Measuring and modeling the effect of surface moisture on the spectral reflectance of coastal beach sand. PLoS One 9 (11), e112151.
Nordstrom, K.F., 2004. Beaches and Dunes of Developed Coasts. Cambridge University Press.
Nordstrom, K.F., Jackson, N.L., 1998. Effects of a high rise building on wind flow and beach characteristics at Atlantic City, NJ, USA. Ocean Coast. Manag. 39 (3), 245–263.
Nordstrom, K.F., McCluskey, J.M., 1984. Considerations for control of house construction in coastal dunes. Coast. Manag. 12 (4), 385–402.
Nordstrom, K.F., McCluskey, J.M., 1985. The effects of houses and sand fences on the eolian sediment budget at Fire Island, New York. J. Coast. Res. 39–46.
Paola, C., Voller, V.R., 2005. A generalized Exner equation for sediment mass balance. J. Geophys. Res. Earth 110 (F4).
Peterka, J.A., Meroney, R.N., Kothari, K.M., 1985. Wind flow patterns about buildings. J. Wind Eng. Ind. Aerodyn. 21 (1), 21–38.
Poppema, D.W., Wijnberg, K.M., Mulder, J.P.M., Vos, S.E., Hulscher, S.J.M.H., 2021. The effect of building geometry on the size of aeolian deposition patterns: Scale model experiments at the beach. Coast. Eng. 168, 103866.
Poppema, D.W., Wijnberg, K.M., Mulder, J.P.M., Hulscher, S.J.M.H., 2022. Deposition patterns around buildings at the beach: Effects of building spacing and orientation. Geomorphology 401, 108114.

Pourteimouri, P., Campmans, G.H., Wijnberg, K.M., Hulscher, S.J., 2021. A Numerical study on the impact of building dimensions on airflow patterns and bed morphology around buildings at the beach. J. Marine Science Eng. 10 (1), 13.
Pye, K., Tsoar, H., 1990. Aeolian Sand and Sand Dunes. Unwin Hyman, London, p. 396.
Qian, G., Dong, Z., Luo, W., Lu, J., 2011. Mean airflow patterns upwind of topographic obstacles and their implications for the formation of echo dunes: A wind tunnel simulation of the effects of windward slope. J. Geophys. Res. Earth 116 (F4).
Richards, P.J., Hoxey, R.P., 1993. Appropriate boundary conditions for computational wind engineering models using the k-ϵ turbulence model. J. Wind Eng. Ind. Aerodyn. 46, 145–153.
Shah, K.B., Ferziger, J.H., 1997. A fluid mechanicians view of wind engineering: Large eddy simulation of flow past a cubic obstacle. J. Wind Eng. Ind. Aerodyn. 67, 211–224.
Silva, F.G., Wijnberg, K.M., de Groot, A.V., Hulscher, S.J.M.H., 2018. The influence of groundwater depth on coastal dune development at sand flats close to inlets. Ocean Dyn. 68 (7), 885–897.
Tominaga, Y., Okaze, T., Mochida, A., 2018. Wind tunnel experiment and CFD analysis of sand erosion/deposition due to wind around an obstacle. J. Wind Eng. Ind. Aerodyn. 182, 262–271.
Tsoar, H., 1983. Wind tunnel modeling of echo and climbing dunes. In: Developments in Sedimentology, Vol. 38. Elsevier, pp. 247–259.
Unnikrishnan, S., Ogunremi, A., Sumner, D., 2017. The effect of incidence angle on the mean wake of surface-mounted finite-height square prisms. Int. J. Heat Fluid Flow 66, 137–156.
Walker, I.J., Nickling, W.G., 2002. Dynamics of secondary airflow and sediment transport over and in the lee of transverse dunes. Prog. Phys. Geogr. 26 (1), 47–75.
Yakhot, A., Liu, H., Nikitin, N., 2006. Turbulent flow around a wall-mounted cube: A direct numerical simulation. Int. J. Heat Fluid Flow 27 (6), 994–1009.
Yen, S.C., Liu, C.T., 2011. Gap-flow patterns behind twin-cylinders at low Reynolds number. J. Mech. Sci. Technol. 25 (11), 2795–2803.

Further reading

Blocken, B., Stathopoulos, T., Carmeliet, J., Hensen, J.L., 2011. Application of computational fluid dynamics in building performance simulation for the outdoor environment: an overview. J. Build. Perform. Simul. 4 (2), 157–184.
Cheng, H., Castro, I.P., 2002. Near wall flow over urban-like roughness. Bound.-Lay. Meteorol. 104 (2), 229–259.
Meroney, R.N., Pavageau, M., Rafailidis, S., Schatzmann, M., 1996. Study of line source characteristics for 2-D physical modelling of pollutant dispersion in street canyons. J. Wind Eng. Ind. Aerodyn. 62 (1), 37–56.
Oke, T.R., Mills, G., Christen, A., Voogt, J.A. (Eds.), 2017. Urban Climates. Cambridge University Press.